Title
Metal–oxygen decoordination stabilizes anion redox in Li-rich oxides

Journal
Nature Materials, 18(3)

ISSN
1476-1122

Authors
Hong, Jihyun
Gent, William E
Xiao, Penghao
et al.

Publication Date
2019-03-01

DOI
10.1038/s41563-018-0276-1

Peer reviewed

Metal-Oxygen Decoordination Stabilizes Anion Redox in Li-rich Oxides

Authors: Jihyun Hong[1,2,3,4§,†], William E. Gent[5,6†], Penghao Xiao[7], Kipil Lim[1,2,3,4], Dong-Hwa Seo[8], Jinpeng Wu[3,6], Peter M. Csernica[1], Christopher J. Takacs[2], Dennis Nordlund[2], Cheng-Jun Sun[9], Kevin H. Stone[2], Donata Passarello[2], Wanli Yang[6], David Prendergast[10], Gerbrand Ceder[7,8]*, Michael F. Toney[2,4]*, William C. Chueh[1,3,4]*

Affiliations:

[1] Department of Materials Science and Engineering, Stanford University, 496 Lomita Mall, Stanford, CA 94305, U.S.A.

[2] Stanford Synchrotron Radiation Lightsource, SLAC National Accelerator Laboratory, 2575 Sand Hill Road, Menlo Park, CA 94025, U.S.A.

[3] Stanford Institute for Materials & Energy Sciences, SLAC National Accelerator Laboratory, 2575 Sand Hill Road, Menlo Park, CA 94025, U.S.A.

[4] Applied Energy Division, SLAC National Accelerator Laboratory, 2575 Sand Hill Road, Menlo Park, CA 94025, U.S.A.

[5] Department of Chemistry, Stanford University, 333 Campus Drive, Stanford, CA 94305, U.S.A.

[6] The Advanced Light Source, Lawrence Berkeley National Laboratory, 1 Cyclotron Road, Berkeley, CA 94720 U.S.A.

[7] Materials Sciences Division, Lawrence Berkeley National Laboratory, 1 Cyclotron Road, Berkeley, CA 94720, U.S.A.

[8] Department of Materials Science and Engineering, University of California, Berkeley, 2607 Hearst Ave, Berkeley, CA 94720, U.S.A.

[9] The Advanced Photon Source, Argonne National Laboratory, 9700 Cass Ave, Lemont, IL 60439, U.S.A.

[10] The Molecular Foundry, Lawrence Berkeley National Laboratory, 1 Cyclotron Road, Berkeley, CA 94720, U.S.A.

[§] Present address: High-Temperature Energy Materials Research Center, Korea Institute of Science and Technology (KIST), Seoul, 02792, Republic of Korea.

* Correspondence to: gceder@berkeley.edu, wchueh@stanford.edu, mftoney@slac.stanford.edu

[†] Equal contribution authors.

Abstract:

Reversible high voltage redox chemistry is an essential component of many electrochemical technologies, from (electro)catalysts to lithium-ion batteries. Oxygen anion redox has garnered intense interest for such applications, particularly lithium ion batteries, as it offers substantial redox capacity at > 4 V vs. Li/Li^+ in a variety of oxide materials. However, oxidation of oxygen is almost universally correlated with irreversible local structural transformations, voltage hysteresis, and voltage fade, which currently preclude its widespread use. By comprehensively studying the $Li_{2-x}Ir_{1-y}Sn_yO_3$ model system, which exhibits tunable oxidation state and structural evolution with *y* upon cycling, we reveal that this structure-redox coupling arises from the local stabilization of short ~ 1.8 Å metal-oxygen π bonds and ~ 1.4 Å O–O dimers during oxygen redox, which occurs in $Li_{2-x}Ir_{1-y}Sn_yO_3$ through ligand-to-metal charge transfer. Crucially, formation of these oxidized oxygen species necessitates the decoordination of oxygen to a single covalent bonding partner through formation of vacancies at neighboring cation sites, driving cation disorder. These insights establish a point defect explanation for why anion redox often occurs alongside local structural disordering and voltage hysteresis during cycling. Our findings offer an explanation for the unique electrochemical properties of lithium-rich layered oxides, with implications generally for the design of materials employing oxygen redox chemistry.

Main Text:

Reversible redox chemistry in solids under highly oxidizing conditions (e.g. vs H_2/H^+, Li/Li^+, or O_2) is a powerful tool in (electro)chemical systems, increasing the catalytic activity of oxygen-evolution and methane-functionalization (electro)catalysts as well as the energy and power densities of lithium-ion batteries (LIBs).[1] In LIBs in particular, employing high-voltage redox has been identified as a promising avenue to meeting the energy density demands of next-generation technologies such as plug-in electric vehicles.

Recently, anionic oxygen redox has been shown to offer access to substantial high-voltage (de)intercalation capacity in a range of electrode materials,[2-7] spurring an intense research effort to understand this phenomenon. While many oxygen-redox-active materials have been developed, they almost universally exhibit a host of irreversible electrochemical behaviors such as voltage hysteresis and voltage fade.[8] This is most notable in the anion-redox-active Li-rich layered oxides, $Li_{1+x}M_{1-x}O_2$ (M = a transition metal (TM) or non-transition metal such as Al, Sn, Mg, etc.), which exhibit capacities approaching 300 mAh g^{-1} but have yet to achieve commercial success due to such electrochemical behaviors.[5, 9] It has been shown both experimentally[10-12] and from first-principles thermodynamics[13] that the migration of M into empty Li sites[9] – creating structural disorder in the form of M_{Li}/V_M antisite/cation vacancy point defect pairs – is at the root of voltage profile evolution and depression, particularly during the first cycle. Oxygen redox has separately been shown to trigger voltage hysteresis and sluggish kinetics,[8, 14] with the implication being that oxygen redox and transition metal (TM) migration/vacancy formation are often intrinsically linked. Indeed, the coupling between oxygen redox, cation migration, and voltage hysteresis was recently observed.[6] However, under the two primary models that have emerged to describe the nature of the lattice oxygen in these materials (either a ~ 2.5 Å peroxo-like O_2^{n-}

dimer[3, 15] or an isolated O^- anion[4, 5, 16]), it is unclear as to why the oxidation of oxygen should lead to the correlated structural transformations and voltage hysteresis. It has been argued qualitatively that the oxidation of oxygen destabilizes the layered structure;[2, 15] however, a robust understanding of the materials design criteria for achieving structurally and electrochemically reversible anion redox remains elusive.

In approaching this issue, we turn to layered Li_2IrO_3 (equivalently, $Li[Li_{0.33}Ir_{0.67}]O_2$ or LIO) which is reported to exhibit anion redox, yet, unlike other Li-rich layered oxides, exhibits highly reversible structural and electrochemical behavior during cycling.[15, 17] Upon substituting redox-inactive Sn for Ir, the solid solution material $Li_2Ir_{1-y}Sn_yO_3$ (LISO) forms M_{Li}/V_M defects during charge, accompanied by voltage hysteresis during subsequent cycling that is typical of other anion-redox-active oxides.[15] This tunability makes LIO/LISO an ideal model system for studying the link between anion redox, local structure, and irreversible electrochemistry.

In this work, we show that the difference in electrochemical and structural behavior between LIO and LISO holds the key to understanding anion redox. Using a combination of bulk-sensitive spectroscopic and structural probes in conjunction with first principles calculations, we demonstrate that anion redox only occurs simultaneously with structural disordering (i.e. antisite/vacancy formation) in LISO, and is completely absent in LIO up to 4.6 V, further establishing the strong coupling between these two phenomena. We demonstrate that the ~ 2.5 Å O–O dimers that form in LIO do not constitute oxidized oxygen, and that the high degree of covalency and the low voltage of the Ir redox states together prevent oxygen redox from being accessed in LIO. Crucially, we reveal the origin of the coupling between structural evolution and oxygen redox in LISO using density-functional theory (DFT) calculations, wherein the low valence electron count in delithiated LISO promotes charge transfer from O to Ir (essentially,

oxygen oxidation *via* ligand to metal charge transfer, or LMCT) through drastic changes in the local bonding configuration. We identify two main bonding configurations that are able to stabilize both the low valence electron count through LMCT and the resulting oxidized oxygen species: short ~ 1.8 Å Ir-O π bonds (equivalently, terminal Ir=O oxo species) and short ~ 1.4 Å O–O dimers. Both configurations require the decoordination of oxygen down to a single covalent bonding partner, which is realized in the layered structure through vacancy formation due to in-plane and out-of-plane site disorder (cation migration). Meanwhile, the higher valence electron count in LIO disfavors LMCT and thus LIO exhibits minimal structural disordering, cation redox only, and more reversible electrochemistry. While further investigation is needed to understand how this mechanism depends on the nature of the TM, this point defect model can offer a causal explanation for the nearly universal observation of structural and electrochemical irreversibility in anion-redox-active Li-rich materials and reveals previously unconsidered design parameters through which to improve them, such as the electronic and structural mechanism of LMCT and oxygen decoordination. These principles apply generally to the design of the broad class of highly oxidized oxides where anion redox is likely to play a role.

Electrochemistry and phase behavior of Li_2IrO_3

As previously reported,[15, 17] Fig. 1a shows that LIO exhibits two well-defined voltage plateaus with average potentials of 3.45 V and 4.15 V versus Li/Li^+ and a total capacity of $1.5e^-$ per Ir. It was previously shown that LIO exhibits a layered structure with monoclinic *C2/m* symmetry, with the Li and TMs in the TM layers ordered into a honeycomb-like arrangement, and accommodates delithiation through changes in the stacking of the TM layers, changing from initially O3 to O1[18] at the end of charge. This is further supported here by Rietveld refinement of

the synchrotron X-ray diffraction (XRD) patterns (figs. S1 & S2, tables S1 & S2, and Supplementary discussion S1). In addition, we identify the intermediate Li_1IrO_3 phase as exhibiting T3 stacking using DFT (Fig. S3). We note that the material studied here exhibits a high degree of initial structural ordering and electrochemical reversibility, and is therefore more similar to that reported by Kobayashi et al.[17] than McCalla et al.[15]

While it was previously shown that LIO exhibits minimal structural disordering during the first charge, for this study it is important to quantify the cation vacancy/antisite formation during electrochemical cycling such that it can be compared to LISO. We employed an iterative approach to simultaneously refine the in-plane and out-of-plane site disorder as described in Supplementary discussion S1 and Fig. S4. This approach eliminates the difficulty in site occupancy determination resulting from the presence of stacking faults. We confirm the absence of V_{Ir}/Ir_{Li} defects ($\leq 0.1\pm0.2\%$ of all Li sites occupied by Ir) in the discharged state both before and after the first electrochemical cycle. In-plane site occupancy refinement of the fully charged O1 structure is challenging due to distortions to the oxygen sublattice[15] and the absence of superstructure peaks. However, out-of-plane refinement shows negligible Ir occupancy in the Li layer in the fully charged state. Consistently, DFT calculations indicate that in-plane and out-of-plane Ir antisite/vacancy defect pairs in the fully charged state have a positive formation energy of +0.49 and +0.20 eV (per $Li_4Ir_8O_{24}$ supercell), respectively. Together, these results show why LIO exhibits reversible electrochemistry: minimal cation disordering occurs during cycling. This is unlike most other Li-rich materials in which anion redox is reported to occur.[7, 9, 12, 19]

Multivalent iridium redox in Li_2IrO_3

The nature of anion redox in LIO should therefore be examined with further scrutiny. In addition, a strict definition of anion redox is needed. Until now, oxygen redox has been defined as the depopulation of non-bonding (or "weakly/minimally hybridized") oxygen 2p states[5, 6, 16, 20, 21]. However, this definition does not take into account how materials respond to the depopulation of these states, which as we will show later is a crucial component of oxygen redox. So, we provide a more specific definition here: oxygen redox requires the depopulation of non-bonding (or "weakly/minimally hybridized") oxygen *2p* states wherein the resulting holes reside in predominantly oxygen character orbitals after any structural and electronic reorganization has occurred. A previous study reported anion redox in LIO based on: (a) surface-sensitive X-ray photoelectron spectroscopy (XPS) showing the appearance of an oxygen state with reduced electron density, and (b) neutron diffraction and transmission electron microscopy (TEM) measurements showing the contraction of the octahedral O–O distance from ~2.7 Å to ~2.5 Å.[15] Here we use bulk-sensitive X-ray spectroscopic techniques to directly determine the nature of the hole states formed during charge and, by induction, the redox processes in LIO. We first show in Fig. 1 analysis of the *operando* transmission X-ray absorption near edge structure (XANES) at the Ir L_3 edge during the first cycle of LIO.[19, 22, 23] Figure 1b shows that the white line (WL) energy increases linearly during the galvanostatic charge up to $Li_{0.5}IrO_3$ and then decreases linearly on discharge, nearly returning to its original value after the full cycle. Figure 1c, meanwhile, shows that the WL intensity increases up to Li_1IrO_3 but then decreases when charging further to $Li_{0.5}IrO_3$, with the trend reversing on discharge. Principal component analysis and non-negative matrix factorization (NMF) of the XANES spectra (Supplementary discussion S2 and Fig. S5) reveal the presence of three spectral end members corresponding to the Li_2IrO_3, Li_1IrO_3, and $Li_{0.5}IrO_3$ compositions, consistent with the presence of two isosbestic points. These

three end member spectra (Fig. 1d, inset) reflect the observed changes, with $Li_{0.5}IrO_3$ having the highest WL energy followed by Li_1IrO_3 and Li_2IrO_3, and with Li_1IrO_3 having the strongest WL peak intensity. A linear combination analysis (LCA) using these end members confirms that the entire spectral evolution is well described by two consecutive two-phase reactions between Li_2IrO_3 and Li_1IrO_3, and between Li_1IrO_3 and $Li_{0.5}IrO_3$ (figs. 1d and S5).

To understand what these spectral changes indicate, we note that the L_3 WL energy has been shown to vary linearly with formal Ir oxidation state.[34] Thus the linear trend during galvanostatic cycling indicates a linear, monotonic change in Ir oxidation state, with a total WL shift of 1.2 eV. The Ir WL energy difference between Ir^{6+} and Ir^{4+} compounds is typically between 1.4-2.0 eV,[23, 24] and the WL shift here is therefore consistent with Ir being oxidized by between 1.2-1.7 e^-. Although it was argued that a loss in WL intensity indicates Ir reduction in Li_3IrO_4,[19] it has been shown that the WL intensity of Ir^{6+} is lower than that of Ir^{5+},[23, 24] which may be due to the WL intensity becoming dominated by relaxation quenching rather than d count for d counts below d^4-d^5.[25] Thus both the WL energy and intensity suggest a monotonic oxidation of Ir from 4+ to between 5.2+ and 5.7+.

Since the linear coefficient between WL energy and oxidation state appears to vary slightly between materials,[23, 24] it is impossible to precisely quantify the final Ir oxidation state based on XANES studies in other materials. Thus, although the monotonicity of the Ir oxidation is already in striking contrast to the behavior of most anion redox active Li-rich oxides, whose TM ions either stop being oxidized or are even reduced during the high voltage plateau,[4, 6, 16] and suggests the absence of anion redox in LIO and a final Ir oxidation state of 5.5+, this cannot be proven with XANES alone. To directly assess the contribution of bulk O to the LIO redox mechanism, we perform soft X-ray absorption spectroscopy (sXAS) at the O K edge. Transmission and

fluorescence yield (FY) detection modes with probing depths of hundreds of nm were employed (see methods). Figure 2a shows the O K edge sXAS-FY and transmission sXAS spectra of LIO (initially in the $t_{2g}^5 e_g^0$ electronic configuration) during the first electrochemical cycle. The peaks at ~529 eV and 532 eV are ascribed to the unoccupied Ir 5*d*-O 2*p* t_{2g} and e_g^* hybridized states, respectively.[26, 27] The difference plots taken between different states of charge (Fig. 2b) clearly show that the intensity of the t_{2g} peak increases and decreases throughout charge and discharge, mirroring the evolution of the Ir L_3 WL (Fig. 1c). Figure 2c shows that the integrated area ratio of the two O K XAS pre-edge peaks follows the same trend in transmission sXAS, which probes the entirety of the particles, confirming that this is a bulk phenomenon.

The correlated changes at the O K and Ir L_3 edges indicate redox of a hybridized Ir–O state, and are widely accepted as a fingerprint of conventional "TM–O" cation redox[6] observed in a variety of compounds such as $LiNi_{0.5}Mn_{1.5}O_4$,[28] $LiFePO_4$,[29] *3d* layered TM oxides.[6, 26] While in these systems the oxidation of the TM is accompanied by charge sharing with the anions, this clearly does not qualify as oxygen redox according to the earlier definition since no *additional* unhybridized O *2p* electrons are depopulated beyond the hybridized TM–O states. This is further supported by resonant inelastic X-ray scattering (RIXS) at the O K edge. It has recently been shown that depopulation of unhybridized O *2p* states in some Li-rich materials results in a sharp absorption feature at ~ 530.8 eV excitation energy at the O K edge with a characteristic emission at ~ 523.0 eV, evident in both RIXS maps[6] and single-energy RIXS spectra,[6, 16, 30, 31] which is distinct from the energy of typical hybridization features in most TM oxides. Figure 2d shows, however, that no such feature appears even in the fully charged LIO. Thus, in conjunction with the XANES results, O K edge sXAS and RIXS further support pure multivalent, hybridized Ir–O redox in the absence of oxygen redox in LIO.

This is also supported by DFT calculations. The predicted projected density of states (pDOS) of the oxygen *2p* and Ir *5d* states of the three structures formed during cycling are shown in Fig. 2e. Changes in the Ir and O pDOS as a function of Li stoichiometry show that all states depopulated during delithiation contain both Ir and O character. The unhybridized O *2p* states (*i.e.*, the non-bonding (NB) O *2p* band) lie ~ 2 eV below the Fermi level in $Li_{0.5}IrO_3$ and are therefore not emptied. Insets in Fig. 2e plot the isosurface of the spin density of the lowest unoccupied (*i.e.*, redox active) states around Ir and O for Li_1IrO_3 and $Li_{0.5}IrO_3$. (equivalent to 0.5 electrons per formula unit, shaded in the DOS). In both cases, we observe large spin density around both Ir and O ions in the shape of two distinct hybridized Ir *5d*-O *2p* t_{2g} orbitals – likely d_{xy} and mixed d_{yz}-d_{xz}. Thus, although all oxygen ions in LIO exhibit the linear Li–O–Li structural motif that was recently shown to raise the energy of the O 2*p* states and promote oxygen redox in many Li-rich materials (see Fig. S6),[5, 6, 32] these results demonstrate that the $Ir^{4/5.5+}$ redox band (where 5.5 denotes the average formal oxidation state) is too high in energy for these labile O 2*p* states to compete for redox in LIO, similar to predictions made for V, Cr, and Mo.[5]

Having employed a suite of bulk-sensitive spectroscopic probes and computation, we show that only hybridized TM–O states are accessed in LIO, with Ir reaching the 5.5+ formal oxidation state at the end of charge. We therefore re-classify LIO as anion-redox inactive within the 2.5-4.6 V window. In terms of addressing previous conflicting conclusions, it is likely that the oxidized oxygen species observed by XPS are due to near-surface phenomena which do not play a significant role in the bulk redox mechanism. As for the long ~ 2.5 Å O–O dimers that were observed to form in the bulk of charged LIO, we conclude that these species are not sufficient evidence of oxidized oxygen. This is based on the observation that most TM-coordinated

oxidized oxygen dimers are between 1.3-1.5 Å in length.[33] We speculate on alternative explanations for the dimerization phenomenon in Supplementary discussion S3 and Fig. S7.

Extra capacity beyond $Ir^{5.5+}$ in LISO and irreversible electrochemical/structural evolution

When Sn is substituted into Li_2IrO_3 to make solid-solution phase $Li_2Ir_{1-y}Sn_yO_3$, the electrochemistry changes dramatically and becomes typical of that of anion redox active materials (Fig. 3a). We use the notation LISO## to represent the compound with ## % Sn content, and the term "LISO" to refer to the Sn-substituted materials generally. Regardless of Sn content, when charged beyond $Ir^{5.5+}$, LISO exhibits a new plateau at ~ 4.35 V, followed by a large voltage drop on the subsequent discharge, a permanently sloped voltage profile, and voltage hysteresis that persists even at open circuit (Fig. S8). Despite the drastic changes to the voltage profile, LISO25 exhibits reasonable capacity retention with cycling (74.5% after 192 cycles, Fig. S9). The new high voltage plateau, in conjunction with the additional reversible capacity well beyond 1.5 e^- per Ir (Fig. 3a), indicates the presence of a reversible redox partner beyond $Ir^{4+}/Ir^{5.5+}$.

In addition to this high-voltage redox partner, the average and local structural behavior of LISO differs from that of LIO. As first demonstrated by McCalla *et al.*,[15] a substantial degree of cation site disorder develops in LISO after first delithiation. Figure 3b quantifies the extent of site disorder in LISO25 before and after electrochemical cycling with either a 4.25 or 4.60 V cutoff. The iterative Rietveld refinement results are shown in Fig. S10 and tables S3 & S4. As shown schematically in Fig. 3b, we assume that each in-plane and out-of-plane antisite defect results in a corresponding vacant M site (V_M). Since low concentrations of Sn_{Li} and Ir_{Li} have an identical effect on the Bragg peak intensity, XRD cannot be used to differentiate between the migrating

256 species. We therefore perform the refinement assuming either all Ir_{Li} for both in-plane and out-
257 of-plane defects or only Sn_{Li} for out-of-plane defects and Ir_{Li} for in-plane defects (assuming all
258 Sn_{Li} for both types of defect leads to full depletion of the Sn content in the M sites in LISO25).
259 We quantify the total amount of disorder by the fraction of V_M, which reaches between
260 8.97±0.9% (assuming all Ir_{Li} defects) and 12.0±1.4 % (assuming Sn_{Li} for out-of-plane defects
261 and Ir_{Li} for in-plane defects) after a single cycle between 4.60-2.50 V, approximately evenly split
262 between in-plane and out-of-plane antisite defects. Since the total accessed capacity is
263 approximately the same between LIO and the various LISO compositions, by substituting with
264 Sn we can conclude that the structural disordering is not due to global structural instability
265 caused by low lithium contents. Instead, the disordering appears to be associated with the new
266 redox partner giving rise to the high voltage plateau: the disorder in LISO25 after a full cycle is
267 dramatically greater than in both LIO after the first cycle and LISO25 after a single cycle
268 between 4.25-2.50 V, which are both zero within experimental error. Out-of-plane refinement of
269 the fully charged O1 structure shows that the disorder is increased substantially at 4.60 V (tables
270 S3 & S4), providing a direct connection between the new redox partner, electrochemical
271 irreversibility, and the onset of cation disordering. Increased cation disordering with increased
272 redox capacity beyond $Ir^{4+/5.5+}$ is further supported by pair distribution function (PDF) analysis
273 (figs. S11-S14 and table S5) and EXAFS at the Ir L_3 edge (Fig. S15), which shows that the
274 decrease in scattering intensity of the first and second coordination shells during charge in LISO
275 – indicative of disorder in the atomic distances – is more substantial when the fraction of
276 capacity beyond $Ir^{4+/5.5+}$ is greater (i.e. with increasing Sn content). The changes to the XRD
277 pattern in charged LISO50 (Fig. S16) are complex and make reliable quantification of
278 occupancies with Rietveld refinement challenging. However, refinement in the discharged state

(tables S6 & S7) and the PDF and EXAFS behavior are similar to, and show more extensive disordering than, LISO25. As discussed later, DFT also consistently predicts more favorable in-plane and out-of-plane cation migration in fully charged LISO compared to LIO, further supporting cation disordering during charge.

O redox switched on by Sn substitution

The electrochemical and structural data confirm that Sn substitution turns on an additional high voltage redox partner that is associated with M_{Li}/V_M defect formation and voltage hysteresis. To further probe the nature of the high voltage LISO redox partner, we perform *operando* transmission XAS at the Ir L_3 and Sn K edges and RIXS at the O K edge. Figures 3c and S17a show that, as with LIO, charging to 4.25 V results in a shift to higher energy of the Ir L_3 WL energy. This is correlated with an increase in intensity of the Ir *5d*-O *2p* t_{2g} peak at the O K edge (Fig. 3d), confirming that this is standard hybridized Ir–O redox. Strikingly, the Ir L_3 WL energy is essentially unchanged when charging beyond 4.25 V, exhibiting only a slight decrease in the peak intensity (Fig. S17c). As argued previously, the invariance of the Ir L_3 WL is indicative of a constant oxidation state and thus we rule out continued hybridized Ir-O redox during the high voltage plateau. Figure S17d shows that the Sn K edge absorption changes minimally during charge in LISO25, ruling out the improbable scenario of Sn oxidation beyond 4+.

The constant Ir/Sn oxidation states during the high voltage plateau suggest O redox, and we again turn to the O K edge XAS/RIXS for confirmation. Figure 3d shows that when charging LISO25 from 4.25 to 4.60 V, the t_{2g} peak continues to increase in intensity despite the invariance of the Ir L_3 edge WL. This indicates an increased O 2*p* character in the t_{2g} band without the depopulation of hybridized Ir–O states. Additionally, Fig. 3e shows that when charging to 4.60

V, a sharp RIXS feature at 530.7 eV excitation energy and 523.0 eV emission energy (indicated by the white arrows) emerges. This is seen more clearly in the RIXS emission spectra in Fig. 3f. The feature is strongest in LISO50, which exhibits the greatest extent of high-voltage capacity beyond $Ir^{4+/5.5+}$ (Fig. 3a) and antisite/vacancy defects. This RIXS feature has been observed to closely follow oxygen redox activity in several battery electrodes.[6, 31] Both of these behaviors indicate that, in addition to promoting cation disordering, Sn substitution in LISO also switches on O redox.

Cation migration and O redox stabilized by LMCT *via* short Ir–O π bonding and O–O dimerization

Understanding why Sn substitution gives rise to these phenomena is central to uncovering the origin of the coupling between anion redox and metal migration/vacancy formation. Since the defect concentration is more reliably quantified in LISO25, we focus our DFT analysis on this composition. First, we show in Fig. S18 the evolution of the computed DOS in the control case of ordered, M_{Li}/V_M-free LISO25 as a function of Li stoichiometry. We observe that no unhybridized O *2p* states are depopulated in the fully delithiated O1 structures – only hybridized Ir–O states are accessed, giving Ir a formal oxidation state of at least 6+, which is inconsistent with our XAS results. In fact, the behavior is similar to LIO (albeit more oxidized), with the unhybrdizied O 2*p* states positioned ~1 eV below the Fermi level. Thus, simple delithiation and the O3-O1 stacking change does not explain the high voltage redox process in LISO. Importantly, our DFT calculations suggest that O redox *cannot* occur in LISO after delithiating 1.5 Li per formula unit if M_{Li}/V_M defects are not allowed to form.

Next, we introduce the experimentally-observed Sn_{Li}/V_M defects and examine their effect on the electronic structure and charge distribution of LISO. Out-of-plane Sn migration into a Li layer site creates a cation vacancy, V_M, and neighboring single-coordinate (dangling) oxygen atoms (Fig. S19). Note that we use the term "single-coordinate" to refer to the number of covalent bonding partners – i.e. counting Ir or Sn, but not Li. We find the formation of Sn_{Li}/V_M defect pairs stabilizes the delithiated structure significantly by 1.34-1.36 eV, whereas the formation of Ir_{Li}/V_M defect pairs is predicted to have a much smaller driving force of 0.02 eV.

We attribute the Sn_{Li}/V_M stabilization to the response of the resulting M-O dangling bonds, which undergo one of two major transformations. As shown in Fig. 4a, when M = Ir, these bonds contract substantially, changing from ~2.10 Å to ~1.77 Å. Figure 4b shows that the bond contraction accompanies a splitting of the previously unhybridized O *2p* states (shaded, top panel), with some states moving above the Fermi level and becoming oxidized (shaded, bottom panel). The shifted states, now approximately 1.5 eV higher in energy, rehybridize with the Ir *5d* states. Table S8 shows that the bond contraction results in a donation of charge from the dangling oxygens to the Ir bonding partners. Crystal orbital overlap population (COOP) analysis in Supplementary discussion S4 and Fig. S20 shows that the net bond order between the dangling O and Ir ions increases by 45 % as a result. Together, these observations suggest the formation of short Ir–O π bonds (equivalently, terminal oxo ligands) through donation of oxygen lone pair electrons, approaching Ir=O double bonds although an exact bond order is hard to define in an electronically delocalized crystal. Indeed the substantially shortened Ir–O bonds (1.76 – 1.79 Å) are similar in length to the Ir=O double bond observed in tetrahedral oxotrimesityliridium(V).[34] While short Ir–O π bonding in octahedral environments has not been previously observed in

346 molecular compounds, the low effective Ir^{6+} *d* count (d^3) makes such bonding possible in
347 charged LISO.[35]

348 When M = Sn, on the other hand, the single-coordinate oxygens are predicted to instead pair up
349 to form short (~ 1.44 Å) O–O dimers that straddle the V_M (Fig. 4c and Fig. S19). Again, this
350 transformation results in a shift of the previously buried NB O 2*p* states from below to above the
351 Fermi level (Fig. 4d) along with donation of electron density from O to a neighboring Ir (table
352 S9). We stress that these localized dimers are distinct from the long (~ 2.5 Å) dimers previously
353 proposed for this material[15] in that they are well within the range of typical bond lengths for O_2^{n-}
354 species[33] and, crucially, do not form in the absence of cation migration. These behaviors – the
355 stabilization of the charged structure through Sn migration and Ir=O/O–O formation – are also
356 predicted for LISO50 (Fig. S21). We furthermore note that the computational conclusions are
357 independent of the functional employed (table S10).

358 We note that when both oxygens neighboring the V_M are coordinated to an Ir ion, the short Ir–O
359 π bonds are generally predicted to be more favored than O-O dimers (Fig. S21 and table S10).
360 However, as the Sn content is increased, the fraction of Sn-Sn neighbors increases and thus so
361 does the fraction of Sn-coordinated dangling oxygens after TM migration/vacancy formation,
362 which favor O–O formation (Fig. S21 and table S11). This observation may be due to the
363 increased rotational freedom of the Sn–O bond, facilitating O–O dimerization,[5] as well as the
364 ability of TMs with low d counts (such as $Ir^{5+/6+}$) to adopt terminal oxo ligands in octahedral
365 environments.[35] In addition, in-plane M_{Li}/V_M defect pairs can give rise to the same behavior (Fig.
366 S22).

367 Both the V_M-mediated O–O dimer and short Ir–O bond models are consistent with the local
368 structural evolution measured through EXAFS and PDF. EXAFS (Fig. S15) shows a substantial

decrease in the Ir–O scattering intensity during charge in LISO, which is exacerbated with increasing oxygen redox capacity, consistent with an increased range of Ir–O bond lengths. Meanwhile PDF (Fig. S14) shows a broadening of the M–O nearest neighbor scattering peak in charged LISO, with an increase in scattering intensity at lower radial distance, consistent with the formation of bonds shorter than the octahedral M–O distance of ~ 2 Å.

Additionally, both the O–O dimer and short Ir–O bond mechanisms are supported by the spectroscopy data. Figure 4b predicts the donation of the buried O 2*p* electrons to the over-oxidized Ir ions by raising these buried states above the Fermi level and into the t_{2g} band, preventing Ir from exceeding the 5.5+ oxidation state. This is consistent with the increase in the O K edge t_{2g} peak intensity (Fig. 3d) in the absence of a shift in the Ir L_3 WL energy during oxygen redox (Fig. 3c). Meanwhile, the sharp RIXS feature is associated with specific excitations in highly oxidized states, especially those involving unoccupied O 2*p* states in oxidized oxygen species. Both peroxides[36] and O_2 gas[37] display the same kind of RIXS feature as do charged Li-rich 3*d* layered oxides.[4, 6, 16, 31] Consistently, the formation of O–O dimers presents a mechanism through which the buried O 2*p* states may become unoccupied during delithiation in LISO. While our proposal of O-O is consistent with the RIXS result, we cannot rule out the possibility that different types of oxidized oxygen species may also give rise to a similar feature.

Under our earlier definition, the formation of O_2^{2-} dimers qualifies as oxygen redox since, as shown in Fig. 4, O 2*p* states are shifted above the Fermi level (i.e. depopulated) and end up as the peroxide σ*, which has mostly oxygen character. Thus, this mechanism serves to localize positive charge onto O 2*p* orbitals even in an otherwise highly covalent system. However, in the case of forming short Ir–O π bonds, while the O 2p states are again shifted above the Fermi level, they end up rehybridizing with Ir t_{2g} states. In this case, although this results in additional

capacity beyond $Ir^{4+/5.5+}$, the character of these states, and thus the extent to which this counts as oxygen redox, depends on the TM–O hybridization. While the hybridization may be significant in the LISO materials, the nature of such states could be different in less covalent materials, such as 3*d* TM oxides, and could therefore be important for oxygen redox in other systems.

To understand why LISO undergoes cation migration and oxygen redox while LIO does not, we show in Supplementary discussion S5 that the driving force for forming Sn_{Li}/V_M defect pairs depends strongly on the electron count in LISO, becoming favorable only when this falls below 1.5 e^- per Ir less than that of the pristine material. Thus, it is clear that the driving force for this structure-redox coupling in LISO is the over-oxidation of Ir beyond an average 5.5+ oxidation state. It is also clear that in the two structural transformations described in Fig. 4 (Ir=O and O–O) substantial donation of charge occurs from O to Ir. It has been shown that in Na-ion battery compounds unusually high oxidation states such as Fe^{4+} and Cu^{3+} are stabilized by LMCT, wherein a substantial donation of charge from oxygen to the metal center occurs through strong M–O covalency and low charge transfer energy.[38] We therefore propose that when oxidizing beyond $Ir^{5.5+}$ a sufficiently low charge transfer energy is achieved such that substantial LMCT is promoted and, consequently, new structural motifs and bonding configurations that allow for greater LMCT become stabilized. In the case of Ir=O, the Ir–O bond length is substantially shortened such that the covalency and LMCT is increased (as is clear in figs. 4b and S20 and is well known, for example, for the Mn=O bonds in $KMnO_4$[39]), while in the case of O–O electrons are directly transferred from the O–O σ* to neighboring Ir ions. Figure 5 shows the stepwise process schematically: over-oxidation of Ir through delithiation, followed by Sn migration to create either Ir=O or O–O species with a resulting donation of charge back to Ir, with the net result being oxidation of O. Since the predicted O–O dimer bond length is 1.44 Å, we depict

415 these dimers as peroxide species in Fig. 5. Since the average Ir oxidation state never exceeds
416 5.5+ in LIO, substantial LMCT is not promoted, and therefore LIO exhibits excellent retention of
417 its in-plane and out-of-plane cation order during cycling and no anion redox.

418 Thus, the single-coordinate oxygens simultaneously stabilize both the low valence electron count
419 in charged LISO through LMCT and the resulting oxidized oxygen species, whether they settle
420 as terminal oxo ligands or O–O dimers. Consequently, they promote and stabilize the formation
421 of Sn_{Li}/V_M defects. Importantly, this structure-redox coupling quantitatively accounts for the
422 anion redox capacity. The diffraction results give a V_M concentration in LISO25 of 12.0±1.4%
423 assuming out-of-plane Sn_{Li} defects and in-plane Ir_{Li} defects. This extent of disordering is
424 accompanied by an additional redox capacity of ~0.48 Li beyond $Ir^{4+/5.5+}$. Assuming each
425 decoordinated oxygen contributes one redox electron, this implies that on average ~ 4 oxidized
426 oxygens are generated per migrated atom. Each in-plane and out-of-plane migration pathway
427 studied here generates 4 dangling oxygens, in agreement with this value.

428 We note that the spectroscopic and structural signature of oxidized oxygen in LISO is strikingly
429 similar to that in *3d* and *4d* Li-rich layered oxides.[6, 31] Further work is needed to establish the
430 precise commonalities between 3*d*, 4*d*, and 5*d* Li-rich electrode materials, in particular the
431 mechanism of decoordination and the relative driving force for forming short M–O π bonds
432 versus short ~ 1.44 Å O–O dimers. However, this initially suggests that depopulation of the high-
433 energy O *2p* states lying along the linear Li-O-Li axes of the honeycomb environments in Li-rich
434 layered oxides is generally stabilized through antisite/vacancy formation, short M–O π bonding,
435 and/or short O–O dimerization. Indeed, ab initio molecular dynamics studies have predicted such
436 mechanisms in *3d* Li-rich materials.[40] This also means that the same two-M-coordinate Li-O-Li
437 environments (where M is a covalent, non-alkali cation) that promote oxygen redox by raising

438 the energy of the O 2*p* states also facilitate its stabilization, as only a single M-Li site swap is
439 required to reach single-M-coordinate. In systems such as LISO where these O *2p* states are not
440 sufficiently high lying to be depopulated in the disorder-free state, O redox can still occur if the
441 valence electron count is depleted low enough for substantial LMCT to be promoted via the
442 formation of antisite/vacancy defects, donating the otherwise inaccessible O *2p* electrons to a
443 TM to form the resulting M-O π bonds and O–O dimers.

444 This mechanism contrasts with the conventional thinking that antisite/vacancy formation in Li-
445 rich layered oxides is driven by the destabilization of the layered structure at low Li
446 stoichiometries.[15, 41, 42] We instead propose that this defect behavior is best understood as an
447 overall decoordination of oxygen in response to low valence electron counts and/or oxygen
448 redox. Indeed, this explains why the onset of electrochemical irreversibility for wide a range of
449 Sn content coincides with exceeding the $Ir^{5.5+}$ oxidation state and not a specific Li stoichiometry
450 (Fig. 3a). We also emphasize that this decoordination takes the form of both in-plane and out-of-
451 plane cation disorder. This rationalizes early theories of Li-rich layered oxide structural behavior,
452 which proposed a conversion of the honeycomb superstructure to a layered $LiMO_2$ phase via in-
453 plane cation migration,[43] with later studies observing out-of-plane site disorder creating spinel-
454 like structures.[41]

455

456 **Conclusion**

457 In summary, by investigating the effect of Sn substitution in the LIO/LISO model system, we
458 have revealed the origin of the strong coupling between anion redox and structural disordering in
459 Li-rich layered oxides that underlies their irreversible electrochemical properties. We find that
460 LIO exhibits no anion redox, and multivalent hybridized Ir–O redox accounts for the entire

capacity, reconciling why this material exhibits more reversible electrochemical and structural behavior than most known anion-redox-active Li-ion electrode materials. Thus, the long ~ 2.5 Å O–O "dimers" that form in LIO during charge are not evidence of anion redox. When Sn is substituted, the lower valence electron count towards the end of charge promotes substantial LMCT through the formation of short Ir–O π bonds and ~ 1.4 Å O–O dimers, requiring the presence of neighboring cation vacancies and therefore driving the formation of Sn_{Li}/V_M defect pairs. The LMCT realized by the Ir=O and O–O species maintains Ir at its maximum oxidation state of 5.5+ and results, on balance, in O redox. The spectroscopic and structural similarities between O redox in LISO and a range of other Li-rich layered oxides[6, 31, 44] suggest that oxygen redox may be generally stabilized in the local coordination environments created through local structural defects. Although further study is needed to establish the commonalities between materials, this explanation rationalizes the widespread coupling of oxygen redox to cation disordering that gives rise to its irreversible electrochemical properties.

We expect that the nature of the TM=O and O–O species, along with the kinetics and thermodynamics of forming the M_{Li}/V_M defect pair will determine the materials' voltage, long term cycling stability, and rate capability, offering a new framework in which to optimize the performance of Li-rich electrodes. We further suggest that structures outside the layered $Li_{1+x}M_{1-x}O_2$ framework that can accommodate the formation of short O–O and/or TM=O bonds through small distortions rather than substantial cation rearrangement or, alternatively, materials that can achieve substantial LMCT without drastic structural changes (e.g. through enhanced covalency) could exhibit improved electrochemical and structural reversibility during anion redox. Indeed, in Na-ion layered oxides where interlayer cation migration is limited and possibly even prevented by the large interlayer spacing and/or prismatic interlayer site geometry, structurally

reversible anion redox can be achieved.[45, 46] Given the stabilizing effect of cation migration demonstrated here, the relative reactivity of these materials towards the electrolyte and oxygen evolution in the absence of cation migration will be an interesting avenue of further study. Our results reveal a clear strategy for designing materials for applications beyond energy storage where low valence electron counts (high oxidation states) need to be reversibly accessed, such as catalysts for reactions including oxygen evolution,[20, 47, 48] olefin polymerization,[49] and methane hydroxylation.[50]

References

1. Whittingham MS. Ultimate Limits to Intercalation Reactions for Lithium Batteries. *Chemical Reviews* 2014, **114**(23)**:** 11414-11443.
2. Assat G, Tarascon J-M. Fundamental understanding and practical challenges of anionic redox activity in Li-ion batteries. *Nature Energy* 2018, **3**(5)**:** 373-386.
3. Sathiya M, Rousse G, Ramesha K, Laisa CP, Vezin H, Sougrati MT, *et al.* Reversible anionic redox chemistry in high-capacity layered-oxide electrodes. *Nature Materials* 2013, **12:** 827.
4. Luo K, Roberts MR, Hao R, Guerrini N, Pickup DM, Liu Y-S, *et al.* Charge-compensation in *3d*-transition-metal-oxide intercalation cathodes through the generation of localized electron holes on oxygen. *Nature Chemistry* 2016, **8:** 684.
5. Seo D-H, Lee J, Urban A, Malik R, Kang S, Ceder G. The structural and chemical origin of the oxygen redox activity in layered and cation-disordered Li-excess cathode materials. *Nature Chemistry* 2016, **8:** 692.
6. Gent WE, Lim K, Liang Y, Li Q, Barnes T, Ahn S-J, *et al.* Coupling between oxygen redox and cation migration explains unusual electrochemistry in lithium-rich layered oxides. *Nature Communications* 2017, **8**(1)**:** 2091.
7. Zhan C, Yao Z, Lu J, Ma L, Maroni VA, Li L, *et al.* Enabling the high capacity of lithium-rich anti-fluorite lithium iron oxide by simultaneous anionic and cationic redox. *Nature Energy* 2017, **2**(12)**:** 963-971.
8. Assat G, Delacourt C, Corte DAD, Tarascon J-M. Editors' Choice—Practical Assessment of Anionic Redox in Li-Rich Layered Oxide Cathodes: A Mixed Blessing for High Energy Li-Ion Batteries. *Journal of The Electrochemical Society* 2016, **163**(14)**:** A2965-A2976.
9. Sathiya M, Abakumov AM, Foix D, Rousse G, Ramesha K, Saubanère M, *et al.* Origin of voltage decay in high-capacity layered oxide electrodes. *Nature Materials* 2014, **14:** 230.
10. Dogan F, Long BR, Croy JR, Gallagher KG, Iddir H, Russell JT, *et al.* Re-entrant lithium local environments and defect driven electrochemistry of Li- and Mn-rich Li-ion battery cathodes. *Journal of the American Chemical Society* 2015, **137**(6)**:** 2328-2335.
11. Croy JR, Gallagher KG, Balasubramanian M, Chen Z, Ren Y, Kim D, *et al.* Examining hysteresis in composite $xLi_2MnO_3{\cdot}(1–x)LiMO_2$ cathode structures. *The Journal of Physical Chemistry C* 2013, **117**(13)**:** 6525-6536.
12. Kleiner K, Strehle B, Baker AR, Day SJ, Tang CC, Buchberger I, *et al.* Origin of High Capacity and Poor Cycling Stability of Li-Rich Layered Oxides: A Long-Duration in Situ Synchrotron Powder Diffraction Study. *Chemistry of Materials* 2018, **30**(11)**:** 3656-3667.
13. Abdellahi A, Urban A, Dacek S, Ceder G. The effect of cation disorder on the average Li intercalation voltage of transition-metal oxides. *Chemistry of Materials* 2016, **28**(11)**:** 3659-3665.
14. Konishi H, Hirano T, Takamatsu D, Gunji A, Feng X, Furutsuki S, *et al.* Potential hysteresis between charge and discharge reactions in $Li_{1.2}Ni_{0.13}Mn_{0.54}Co_{0.13}O_2$ for lithium ion batteries. *Solid State Ionics* 2017, **300:** 120-127.
15. McCalla E, Abakumov AM, Saubanère M, Foix D, Berg EJ, Rousse G, *et al.* Visualization of O-O peroxo-like dimers in high-capacity layered oxides for Li-ion batteries. *Science* 2015, **350**(6267)**:** 1516-1521.
16. Luo K, Roberts MR, Guerrini N, Tapia-Ruiz N, Hao R, Massel F, *et al.* Anion redox

chemistry in the cobalt free *3d* transition metal oxide intercalation electrode $Li[Li_{0.2}Ni_{0.2}Mn_{0.6}]O_2$. *Journal of the American Chemical Society* 2016, **138**(35)**:** 11211-11218.

17. Kobayashi H, Tabuchi M, Shikano M, Kageyama H, Kanno R. Structure, and magnetic and electrochemical properties of layered oxides, Li_2IrO_3. *Journal of Materials Chemistry* 2003, **13**(4)**:** 957-962.
18. Delmas C, Braconnier J-J, Fouassier C, Hagenmuller P. Electrochemical intercalation of sodium in Na_xCoO_2 bronzes. *Solid State Ionics* 1981, **3-4**(Supplement C)**:** 165-169.
19. Perez AJ, Jacquet Q, Batuk D, Iadecola A, Saubanère M, Rousse G*, et al.* Approaching the limits of cationic and anionic electrochemical activity with the Li-rich layered rocksalt Li_3IrO_4. *Nature Energy* 2017, **2**(12)**:** 954-962.
20. Grimaud A, Hong WT, Shao-Horn Y, Tarascon JM. Anionic redox processes for electrochemical devices. *Nature Materials* 2016, **15:** 121.
21. Yabuuchi N, Nakayama M, Takeuchi M, Komaba S, Hashimoto Y, Mukai T*, et al.* Origin of stabilization and destabilization in solid-state redox reaction of oxide ions for lithium-ion batteries. *Nature Communications* 2016, **7:** 13814.
22. Choy J-H, Kim D-K, Hwang S-H, Demazeau G, Jung D-Y. XANES and EXAFS Studies on the Ir-O Bond Covalency in Ionic Iridium Perovskites. *Journal of the American Chemical Society* 1995, **117**(33)**:** 8557-8566.
23. Mugavero SJ, Smith MD, Yoon W-S, zur Loye H-C. $Nd_2K_2IrO_7$ and $Sm_2K_2IrO_7$: Iridium(VI) oxides prepared under ambient pressure. *Angewandte Chemie International Edition* 2009, **48**(1)**:** 215-218.
24. Laguna-Marco MA, Kayser P, Alonso JA, Martínez-Lope MJ, van Veenendaal M, Choi Y*, et al.* Electronic structure, local magnetism, and spin-orbit effects of Ir(IV)-, Ir(V)-, and Ir(VI)-based compounds. *Physical Review B* 2015, **91**(21)**:** 214433.
25. Qi B, Perez I, Ansari PH, Lu F, Croft M. L_2 and L_3 measurements of transition-metal *5d* orbital occupancy, spin-orbit effects, and chemical bonding. *Physical Review B* 1987, **36**(5)**:** 2972-2975.
26. Yoon W-S, Balasubramanian M, Chung KY, Yang X-Q, McBreen J, Grey CP*, et al.* Investigation of the charge compensation mechanism on the electrochemically Li-ion deintercalated $Li_{1-x}Co_{1/3}Ni_{1/3}Mn_{1/3}O_2$ electrode system by combination of soft and hard X-ray absorption spectroscopy. *Journal of the American Chemical Society* 2005, **127**(49)**:** 17479-17487.
27. Mortemard de Boisse B, Liu G, Ma J, Nishimura S-i, Chung S-C, Kiuchi H*, et al.* Intermediate honeycomb ordering to trigger oxygen redox chemistry in layered battery electrode. *Nature Communications* 2016, **7:** 11397.
28. Qiao R, Wray LA, Kim J-H, Pieczonka NPW, Harris SJ, Yang W. Direct Experimental Probe of the Ni(II)/Ni(III)/Ni(IV) Redox Evolution in $LiNi_{0.5}Mn_{1.5}O_4$ Electrodes. *The Journal of Physical Chemistry C* 2015, **119**(49)**:** 27228-27233.
29. Liu X, Wang YJ, Barbiellini B, Hafiz H, Basak S, Liu J*, et al.* Why $LiFePO_4$ is a safe battery electrode: Coulomb repulsion induced electron-state reshuffling upon lithiation. *Physical Chemistry Chemical Physics* 2015, **17**(39)**:** 26369-26377.
30. Maitra U, House RA, Somerville JW, Tapia-Ruiz N, Lozano JG, Guerrini N*, et al.* Oxygen redox chemistry without excess alkali-metal ions in $Na_{2/3}[Mg_{0.28}Mn_{0.72}]O_2$. *Nature Chemistry* 2018.
31. Xu J, Sun M, Qiao R, Renfrew SE, Ma L, Wu T*, et al.* Elucidating anionic oxygen

activity in lithium-rich layered oxides. *Nature Communications* 2018, **9**(1)**:** 947.
32. Chen H, Islam MS. Lithium Extraction Mechanism in Li-Rich Li_2MnO_3 Involving Oxygen Hole Formation and Dimerization. *Chemistry of Materials* 2016, **28**(18)**:** 6656-6663.
33. Cramer CJ, Tolman WB, Theopold KH, Rheingold AL. Variable character of O—O and M—O bonding in side-on (η^2) 1:1 metal complexes of O_2. *Proceedings of the National Academy of Sciences* 2003, **100**(7)**:** 3635-3640.
34. Hay-Motherwell RS, Wilkinson G, Hussain-Bates B, Hursthouse MB. Synthesis and X-ray crystal structure of oxotrimesityliridium(V). *Polyhedron* 1993, **12**(16)**:** 2009-2012.
35. Winkler JR, Gray HB. Electronic Structures of Oxo-Metal Ions. In: Mingos DMP, Day P, Dahl JP (eds). *Molecular Electronic Structures of Transition Metal Complexes I*. Springer Berlin Heidelberg: Berlin, Heidelberg, 2012, pp 17-28.
36. Zhuo Z, Pemmaraju CD, Vinson J, Jia C, Moritz B, Lee I*, et al.* Spectroscopic Signature of Oxidized Oxygen States in Peroxides. *The Journal of Physical Chemistry Letters* 2018, **9**(21)**:** 6378-6384.
37. Hennies F, Pietzsch A, Berglund M, Föhlisch A, Schmitt T, Strocov V*, et al.* Resonant Inelastic Scattering Spectra of Free Molecules with Vibrational Resolution. *Physical Review Letters* 2010, **104**(19)**:** 193002.
38. Talaie E, Kim SY, Chen N, Nazar LF. Structural Evolution and Redox Processes Involved in the Electrochemical Cycling of P2–$Na_{0.67}[Mn_{0.66}Fe_{0.20}Cu_{0.14}]O_2$. *Chemistry of Materials* 2017, **29**(16)**:** 6684-6697.
39. Gilbert B, Frazer BH, Belz A, Conrad PG, Nealson KH, Haskel D*, et al.* Multiple Scattering Calculations of Bonding and X-ray Absorption Spectroscopy of Manganese Oxides. *The Journal of Physical Chemistry A* 2003, **107**(16)**:** 2839-2847.
40. Benedek R. First-cycle simulation for Li-rich layered oxide cathode material $xLi_2MnO_3 \cdot (1\text{-}x)LiMO_2$ (x = 0.4). *Journal of The Electrochemical Society* 2018, **165**(11)**:** A2667-A2674.
41. Mohanty D, Li J, Abraham DP, Huq A, Payzant EA, Wood DL*, et al.* Unraveling the Voltage-Fade Mechanism in High-Energy-Density Lithium-Ion Batteries: Origin of the Tetrahedral Cations for Spinel Conversion. *Chemistry of Materials* 2014, **26**(21)**:** 6272-6280.
42. Ceder G, Van der Ven A. Phase diagrams of lithium transition metal oxides: investigations from first principles. *Electrochimica Acta* 1999, **45**(1)**:** 131-150.
43. Thackeray MM, Kang S-H, Johnson CS, Vaughey JT, Benedek R, Hackney SA. Li_2MnO_3-stabilized $LiMO_2$ (M = Mn, Ni, Co) electrodes for lithium-ion batteries. *Journal of Materials Chemistry* 2007, **17**(30)**:** 3112-3125.
44. Okubo M, Yamada A. Molecular Orbital Principles of Oxygen-Redox Battery Electrodes. *ACS Applied Materials & Interfaces* 2017, **9**(42)**:** 36463-36472.
45. Mortemard de Boisse B, Nishimura S-i, Watanabe E, Lander L, Tsuchimoto A, Kikkawa J*, et al.* Highly reversible oxygen-redox chemistry at 4.1 V in $Na_{4/7-x}[\square_{1/7}Mn_{6/7}]O_2$ ($\square$: Mn Vacancy). *Advanced Energy Materials* 2018, **8**(20)**:** 1800409.
46. Rong X, Liu J, Hu E, Liu Y, Wang Y, Wu J*, et al.* Structure-induced reversible anionic redox activity in Na layered oxide cathode. *Joule* 2018, **2**(1)**:** 125-140.
47. Surendranath Y, Kanan MW, Nocera DG. Mechanistic Studies of the Oxygen Evolution Reaction by a Cobalt-Phosphate Catalyst at Neutral pH. *Journal of the American Chemical Society* 2010, **132**(46)**:** 16501-16509.

48. Grimaud A, Diaz-Morales O, Han B, Hong WT, Lee Y-L, Giordano L*, et al.* Activating lattice oxygen redox reactions in metal oxides to catalyse oxygen evolution. *Nature Chemistry* 2017, **9:** 457.
49. Billow BS, McDaniel TJ, Odom AL. Quantifying ligand effects in high-oxidation-state metal catalysis. *Nature Chemistry* 2017, **9:** 837.
50. Snyder BER, Vanelderen P, Bols ML, Hallaert SD, Böttger LH, Ungur L*, et al.* The active site of low-temperature methane hydroxylation in iron-containing zeolites. *Nature* 2016, **536:** 317.

Methods

Materials

Li_2IrO_3 (hereafter, LIO), $Li_2Ir_{0.75}Sn_{0.25}O_3$ (hereafter, LISO25), and $Li_2Ir_{0.5}Sn_{0.5}O_3$ (hereafter, LISO50) were synthesized by solid state reactions. Appropriate amounts of Li_2CO_3 (Alfa Aesar, 99.998% metal basis), IrO_2 (Alfa Aesar, 99.99% metals basis), and SnO_2 (Alfa Aesar 99.9% metals basis) were mixed using a planetary ball mill. 10% excess amount of Li_2CO_3 was used to compensate the lithium evaporation at high temperature. Mixed powder was heat treated at 1000 °C for 12 hours twice in a box furnace with an intermittent grinding, and then naturally cooled to room temperature.

Electrochemical measurements and electrode harvesting

For all electrochemistry figures in this study, 80 wt. % active material, 10 wt.% polyvinylidene fluoride (PVDF) binder (MTI Corporation) and 10 wt. % carbon black (Timcal C65) were mixed with N-methyl-2-pyrrolidone (Acros Organics) and the slurry was cast onto carbon-coated Al foil using a doctor blade. The electrode sheet was dried at 110 °C in air for 1 h followed by overnight at 60 °C under vacuum. Coin cells (CR2032, Wellcos Corporation) were assembled in an Ar filled glove box with a ~11.3 mm diameter LIO/LISO electrode, two 25 µm thick Celgard separators, a 750 µm thick Li foil counter electrode (Sigma-Aldrich), and 1 M $LiPF_6$ in 1:1 (v/v) ethylene carbonate (EC)/diethyl carbonate (DEC) electrolyte (Selectilyte LP 40, BASF). The coin cells were cycled under a constant current density of a C/12 rate (1C = 211 mA g^{-1}_{LIO}, 227.4 mA g^{-1}_{LISO25}, 246.6 mA g^{-1}_{LISO50} corresponding to the (de)lithiation rate of 2Li/h f.u.) between 4.60 V and 2.50 V (LIO and LISO) or 4.25 V and 2.50 V (LISO). Galvanostatic intermittent titration technique (GITT) was applied to measure the open circuit voltage (OCV) at

various states of charge and the thermodynamic voltage hysteresis of LIO and LISO. We applied constant current pulses (C/20) for an hour followed by the relaxation for four hours. This was repeated until the GITT cycle was complete.

Ex situ soft XAS (fluorescence yield), X-ray diffraction (XRD), and resonant inelastic X-ray scattering (RIXS) samples were dismantled from coin cells at the indicated states of charge in an Ar filled glove box. Cells were dismantled using a coin cell decrimping instrument (MTI Corporation). The electrodes were then rinsed with excess DEC and dried under vacuum in the glove box antechamber. For XRD, materials were scraped off of the Al foil current collector and then sealed in a glass capillary (0.5 mm diameter, Ted Pella). All the samples were transferred to the desired instrument in a double-sealed Al-coated polypropylene pouch to prevent air exposure.

X-ray diffraction and Rietveld refinement

High resolution powder XRD patterns for Rietveld refinement were measured at beamline 2-1 at the Stanford Synchrotron Radiation Lightsource (SSRL, SLAC National Accelerator Laboratory) at 17 keV (0.7293 Å) beam energy for as-synthesized powders and at beamline 11-ID-B at the Advanced Photon Source (APS, Argonne National Laboratory) at 58.4 keV (0.2114 Å) beam energy for *ex situ* samples scraped out of electrodes after electrochemical cycling. The size of the X-ray beam was 500 x 1500 μm (SSRL) or 500 x 500 μm (APS). All of the samples were prepared in capillaries to avoid possible preferred orientation of the particles. All of the samples were measured using the transmission geometry.

We used the TOPAS software package (Academic v6, Bruker) for Rietveld refinement. Pawley fitting was employed to determine the crystallographic parameters. The pristine and the samples fully charged to 4.60 V were refined with the *C2/m* space group following previous

687 reports.[15] For the T3-Li_1IrO_3, we found the *Cm* space group to give the best results. For LISO, we
688 assumed that Ir and Sn are randomly distributed through the 4h sites in the TM layer, and the
689 migrated Ir/Sn from 4h was assumed to redistribute equally to the 4g and 2c sites in the Li layer.
690 We allowed variations in the Ir occupancy in Li layer of the fully charged (4.60 V) and fully
691 discharged (2.50 V) LIO and confirmed no Ir migration during the first cycle in LIO.
692
693 X-ray total scattering and pair-distribution function analysis
694 Atomic pair-distribution function (PDF) was analyzed to gain further insights on the local
695 atomic structures of LIO and LISO of the pristine powder and the samples scraped out of the
696 electrodes charged to 4.60 V and discharged to 2.50 V. X-ray total scattering was collected at
697 beamline 11-ID-B at the APS at 58.4 keV (0.2114 Å) beam energy. All of the samples were
698 packed in Kapton capillaries double sealed in Al-coated pouch in an argon filled glove box, and
699 then transferred to the beamline. The pouch was opened right before the measurement to
700 minimize the air exposure. The data collection time was three minutes per sample. We used
701 PDFgetX2 to obtain the atomic PDF from the total scattering data and PDFGUI to fit the atomic
702 PDF from the starting crystal structures determined by Rietveld refinement described above.
703
704 *Operando* Ir L_3 edge XAS and EXAFS spectroscopy
705 For *operando* X-ray absorption spectroscopy (XAS), Al-coated poly propylene (PP) pouch
706 cells containing a ~11.3 mm diameter LIO/LISO electrode, two 25 μm thick Celgard separators,
707 a 250 μm thick Li foil counter electrode (Alfa Aesar), and 1 M $LiPF_6$ in 1:1 (v/v) ethylene
708 carbonate (EC)/diethyl carbonate (DEC) electrolyte (Selectilyte LP 40, BASF), a Ni negative
709 current collector tab, and an Al positive current collector tab were assembled using a tabletop

710 vacuum impulse sealer (Fuji Impulse) in an argon filled glove box. A stainless steel holder with a
711 pair of Be plates (Ted Pella) as an X-ray window was machined to apply a sufficient pressure on
712 the pouch cells using torque screws. The pressure from the stiff windows significantly improved
713 electronic conduction throughout the micro-porous electrodes ensuring homogeneity. The pouch
714 cells were cycled using a portable potentiostat (SP-150, Biologic) under a constant current
715 density of C/12 (where 1C refers to 2Li/h f.u.) between 4.60 V and 2.50 V (*vs.* Li) with 1 hr rest
716 between charge and discharge.

717 The Ir L3 edge XAS spectra of LIO and LISO was collected at beamline 2-2 of Stanford
718 Synchrotron Radiation Lightsource (SSRL) at SLAC National Accelerator Laboratory and
719 beamline 20-BM of the Advanced Photon Source (APS) at Argonne National Laboratory,
720 respectively. The transmission spectra were measured using a 1 x 7 mm unfocused X-ray beam.
721 A Si (220) (SSRL) or Si (111) (APS) crystal monochromator was detuned to 70% of its original
722 intensity to eliminate high order harmonics. Three ion chambers filled with N_2 gas were used in
723 series to simultaneously measure I_0, I_1, and I_{ref}. A Ge reference foil was used to calibrate the
724 photon energy by setting the peak of the first derivative of the K edge absorbance spectrum to be
725 11102 eV. 10 eV, 0.5 eV, and 10 eV energy steps were used in the ranges of 10985-11085 eV,
726 11085.5-11124.5 eV, and 11125-11195 eV, respectively, in order to precisely measure the
727 reference Ge K edge spectra for the calibration followed by the Ir L_3 edge measurement. We
728 used the Athena software package to align and normalize the collected spectra. White line peak
729 was fitted using the sum of an error function and a Lorentzian peak analogous to previous reports.
730 Fourier transformations of k^2 weighted extended X-ray absorption fine-structure (EXAFS)
731 spectra were carried out in the k range from 2 $Å^{-1}$ to 14 $Å^{-1}$ for all the materials.
732

O K edge Soft X-ray Absorption Spectroscopy: FY, RIXS, and transmission

O K edge sXAS of the harvested electrodes were measured in fluorescence yield (FY) mode at SSRL beam line 10-1 equipped with a silicon photodiode detector (AXUV100). Data was acquired under ultrahigh vacuum (10^{-9} Torr) at room temperature with the incident X-ray beam of 500 μm x 500 μm size.

RIXS maps were collected at beam line 8.0.1 at the Advanced Light Source (ALS) in Lawrence Berkeley National Laboratory, using the ultrahigh efficiency iRIXS endstation. All the harvested electrodes were sealed in Al pouches in an argon filled glove box and transferred into a specially designed transfer kit and then the experimental vacuum chamber to avoid air exposure. Technical details of the RIXS beam line and data processing can be found in our previous reports.[6, 51] Two-dimensional emission spectra collected at each excitation energy are aligned using the elastic peak and a reference compound such as TiO_2 to generate the full RIXS maps. The color scale has been tuned in the figures to emphasize the contrast of intensity.

Transmission O K edge sXAS was measured at ALS beam line 11.0.2 using Scanning Transmission X-ray Microscopy. The samples were prepared by sonicating the harvested electrodes in dimethyl carbonate under argon for two hours at room temperature to separate individual particles out of the composite electrodes. The particle suspension was drop-cast onto copper TEM grids with a carbon film (Ted Pella). The grids were loaded onto a sample holder, sealed in an Al-coated pouch, and then transferred to the beam line. We first collected the STXM images with a 50 nm zone plate, an interferometer-controlled stage, and a point detector. The step size was 50 nm and the dwell time for each pixel was typically 1 ms. STXM spectro-images were aligned in the aXis2000 software package. To obtain average absorption spectra, the

aligned absorbance images were filtered at an energy of non-zero intensity, typically 529.5 eV. The pixels below a threshold intensity were set to zero. The remaining un-normalized pixels were then summed to yield the average spectrum. For presentation, normalization of the average spectra was done by subtracting the background intensity and then dividing by the post edge intensity.

Computational details

The calculations for all structures presented were performed with density functional theory (DFT) as implemented in the Vienna *Ab-initio* Simulation Package (VASP).[52, 53] Valence electrons were described by the plane wave basis set and core electrons were incorporated by the projector augmented-wave method.[54-57] Unless otherwise indicated, the perdew-burke-ernzerhof (PBE) functional[58] with the Hubbard *U* correction[59] was adopted for the exchange correlation energy. An effective *U* value of 2.75 eV was applied on Ir.[60] For hybrid calculations, the HSE screened coulomb hybrid density functional[61] was used with a mixing parameter of 0.15 and a range separation parameter of 0.2.[62] The energy cutoff of the plane wave basis was 520 eV and the *k*-point mesh was 3 × 3 × 7 for a 2 × 2 × 1 supercell of O3-$Li_{2-x}MO_3$. Van der Waals interactions were taken into account using the D2 method of Grimme[63] for PBE+U and HSE calculations. For SCAN calculations, the rVV10 non-local van der Waals correlation functional was used.[64] To prepare the structures of $Li_{2-x}IrO_3$, we generated all Li-vacancy orderings within the unit cell of $Li_{2-x}IrO_3$ including 4 formula units using the enumeration technique developed by Hart *et al.*[65, 66] and 10 configurations at x = 1.5 and 0.5 and 100 configurations at x = 1 with lowest electrostatic energy were calculated using GGA. The configurations with the lowest DFT/GGA energy at each Li content were selected as most stable structures. Both octahedral and

tetrahedral sites in Li layer within O3- and O1-Li_xIrO_3 were considered for Li-vacancy orderings at x=1. The same Li-vacancy orderings were applied to the $Li_{2-x}Ir_{0.75}Sn_{0.25}O_3$ case. After Sn migration to Li layer, the Li-vacancy orderings were re-sampled using the basin hopping algorithm.[67]

Data Availability

All experimental data within the article and its Supplementary Information will be made available upon reasonable request to the authors.

References

51. Chuang Y-D, Shao Y-C, Cruz A, Hanzel K, Brown A, Frano A, *et al.* Modular soft x-ray spectrometer for applications in energy sciences and quantum materials. *Review of Scientific Instruments* 2017, **88**(1)**:** 013110.
52. Kresse G, Hafner J. *Ab initio* Moleculare Dynamics for Liquid Metals. *Physical Review B* 1993, **47**(1)**:** 558-561.
53. Kresse G, Hafner J. *Ab initio* Molecular-dynamics Simulation of the Liquid-metal Amorphous-semiconductor Transition in Germanium. *Physical Review B* 1994, **49**(20)**:** 14251-14269.
54. Kresse G, Furthmüller J. Efficient iterative schemes for ab initio total-energy calculations using a plane-wave basis set. *Physical Review B* 1996, **54**(16)**:** 11169-11186.
55. Kresse G, Furthmüller J. Efficiency of ab-initio total energy calculations for metals and semiconductors using a plane-wave basis set. *Computational Materials Science* 1996, **6**(1)**:** 15-50.
56. Blöchl PE. Projector augmented-wave method. *Physical Review B* 1994, **50**(24)**:** 17953-17979.
57. Kresse G, Joubert D. From ultrasoft pseudopotentials to the projector augmented-wave method. *Physical Review B* 1999, **59**(3)**:** 1758-1775.
58. Perdew JP, Burke K, Ernzerhof M. Generalized gradient approximation made simple. *Physical Review Letters* 1996, **77**(18)**:** 3865-3868.
59. Dudarev SL, Botton GA, Savrasov SY, Humphreys CJ, Sutton AP. Electron-energy-loss spectra and the structural stability of nickel oxide: An LSDA+U study. *Physical Review B* 1998, **57**(3)**:** 1505-1509.
60. Subedi A. First-principles study of the electronic structure and magnetism of $CaIrO_3$.

Physical Review B 2012, **85**(2)**:** 020408.
61. Heyd J, Scuseria GE, Ernzerhof M. Hybrid functionals based on a screened Coulomb potential. *The Journal of Chemical Physics* 2003, **118**(18)**:** 8207-8215.
62. Seo D-H, Urban A, Ceder G. Calibrating transition-metal energy levels and oxygen bands in first-principles calculations: Accurate prediction of redox potentials and charge transfer in lithium transition-metal oxides. *Physical Review B* 2015, **92**(11)**:** 115118.
63. Grimme S. Semiempirical GGA-type density functional constructed with a long-range dispersion correction. *Journal of Computational Chemistry* 2006, **27**(15)**:** 1787-1799.
64. Peng H, Yang Z-H, Perdew JP, Sun J. Versatile van der Waals Density Functional Based on a Meta-Generalized Gradient Approximation. *Physical Review X* 2016, **6**(4)**:** 041005.
65. Hart GLW, Forcade RW. Algorithm for generating derivative structures. *Physical Review B* 2008, **77**(22)**:** 224115.
66. Hart GLW, Nelson LJ, Forcade RW. Generating derivative structures at a fixed concentration. *Computational Materials Science* 2012, **59:** 101-107.
67. Wales DJ, Doye JPK. Global optimization by basin-hopping and the lowest energy structures of Lennard-Jones clusters containing up to 110 atoms. *The Journal of Physical Chemistry A* 1997, **101**(28)**:** 5111-5116.

Acknowledgments: This research was supported by the Assistant Secretary for Energy Efficiency and Renewable Energy, Office of Vehicle Technologies, Battery Materials Research Program, U.S. Department of Energy (DOE). WEG was supported additionally by the Advanced Light Source Doctoral Fellowship and the Siebel Scholars program. KL was supported additionally by the Kwanjeong Education Foundation Fellowship. Use of the Advanced Light Source was supported by the Office of Science, Office of Basic Energy Sciences, of the U.S. DOE under Contract No. DE-AC02-05CH11231. Use of the Stanford Synchrotron Radiation Lightsource, SLAC National Accelerator Laboratory, was supported by the Office of Science, Office of Basic Energy Sciences, of the U.S. DOE under Contract No. DE-AC02-76SF00515. Work at the Molecular Foundry was supported by the Office of Science, Office of Basic Energy Sciences, of the U.S. DOE under Contract No. DE-AC02-05CH11231. Part of this work was performed at the Stanford Nano Shared Facilities (SNSF), supported by the National Science Foundation under award ECCS-1542152. This research used resources of the Advanced Photon Source, an Office of Science User Facility operated for the U.S. DOE Office of Science by Argonne National Laboratory, and was supported by the U.S. DOE under Contract No. DE-AC02-06CH11357, and the Canadian Light Source and its funding partners. The computational work was funded by the NorthEast Center for Chemical Energy Storage (NECCES), an Energy Frontier Research Center, supported by the U.S. DOE, Office of Science, Office of Basic Energy Sciences under Award Number DE-SC0012583. GC also thanks China Automotive Battery Research Institute Co., Ltd. and General Research Institute for NonFerrous Metals (GRINM) for financial support on oxygen redox in cathode materials. WEG thanks Ariel Jacobs for insightful discussions on metal-oxygen bonding interactions. The authors thank Karena Chapman (Advanced Photon Source) for valuable comments on X-ray total scattering analysis.

Author Contributions: J.H., W.E.G., W.C.C, and M.F.T. conceived the study. J.H. carried out materials synthesis, characterization and testing. J.H. and K.L. performed ex situ and *operando* synchrotron measurements including XRD, PDF, XAS, sXAS, and RIXS. J.H. and W.E.G. measured ex situ STXM and RIXS spectra. W.E.G., J.W., and W.Y. processed and analyzed spectroscopic data. K.L., J.H., K.H.S., D.Passarello, and M.F.T. performed the structural analyses. K.L., J.H., C.J.T., M.F.T. and W.C.C. designed and constructed settings for in situ synchrotron measurements. P.X., D.-H.S., and G.C. conducted DFT calculations. J.W., K.H.S., D.N., C.S., and K.H. configured synchrotron end stations. P.M.C. provided constructive advice for experiments. J.H., W.E.G., D.Prendergast, W.C.C, and M.F.T. devised the oxygen redox model. J.H., W.E.G., G.C., W.C.C., and M.F.T. wrote the manuscript and all authors revised the manuscript.

Competing Interests: The authors declare no competing interests.

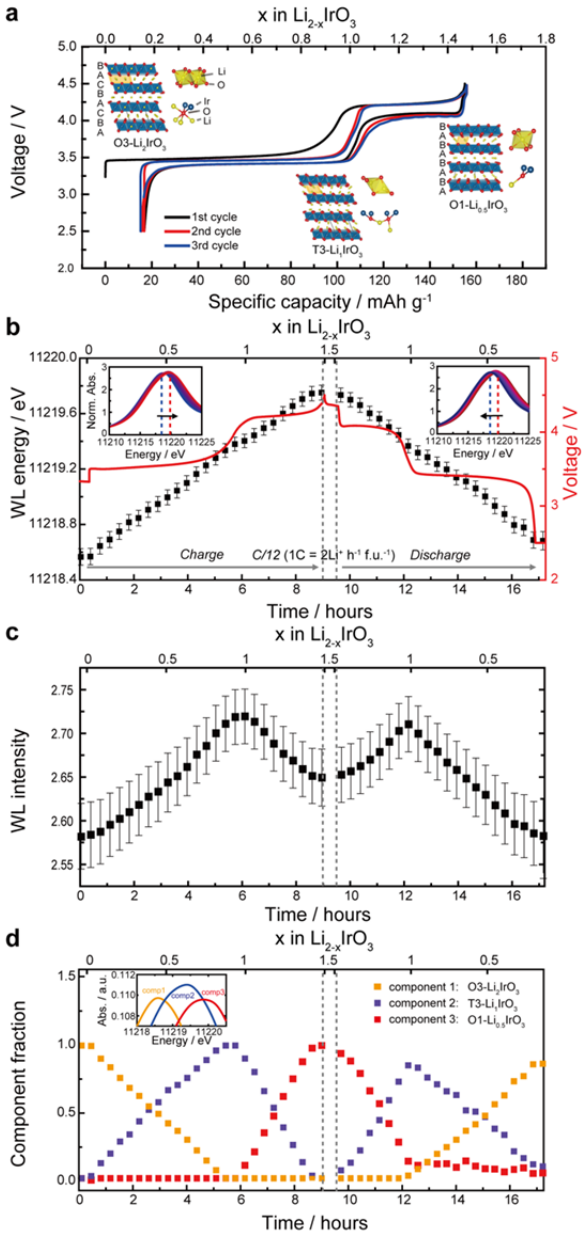

869

870 **Fig. 1. Reversible multivalent iridium redox in $Li_{2-x}IrO_3$.** (**a**) Capacity-voltage curves of Li_{2-}

871 $_xIrO_3$ galvanostatically measured at a C/12 rate (17.58 mA g^{-1}) between 4.50-2.50 V for the

872 initial three cycles. The stable phases during the two consecutive two-phase reactions of $Li_{2-x}IrO_3$

873 occurring at each voltage plateau, obtained by combined XRD Rietveld refinements and DFT

874 calculations, are shown. (**b**) Evolution of the Ir L_3 WL energy (black squares) during the first

875 cycle, measured through *operando* transmission XAS, showing the continuous
876 oxidation/reduction of iridium throughout the whole charge/discharge processes. Error (see
877 methods) was determined to be reasonably small. The raw XANES data for charging and
878 discharging are shown in the left and right insets, respectively. (**c**) Evolution of the Ir L_3 WL
879 intensity, showing the largest intensity at the Li_1IrO_3 composition, where Ir is in the 5+ oxidation
880 state. It is known that Ir^{5+} has a higher WL intensity than Ir^{4+} and Ir^{6+} [23, 24] and thus the
881 subsequent intensity decay is consistent with further oxidation of Ir^{5+} to $Ir^{5.5+}$ during the high
882 voltage plateau at 4.15 V. (**d**) LCA of NMF components, showing three distinct Ir L_3-edge
883 spectra as end members (inset).
884

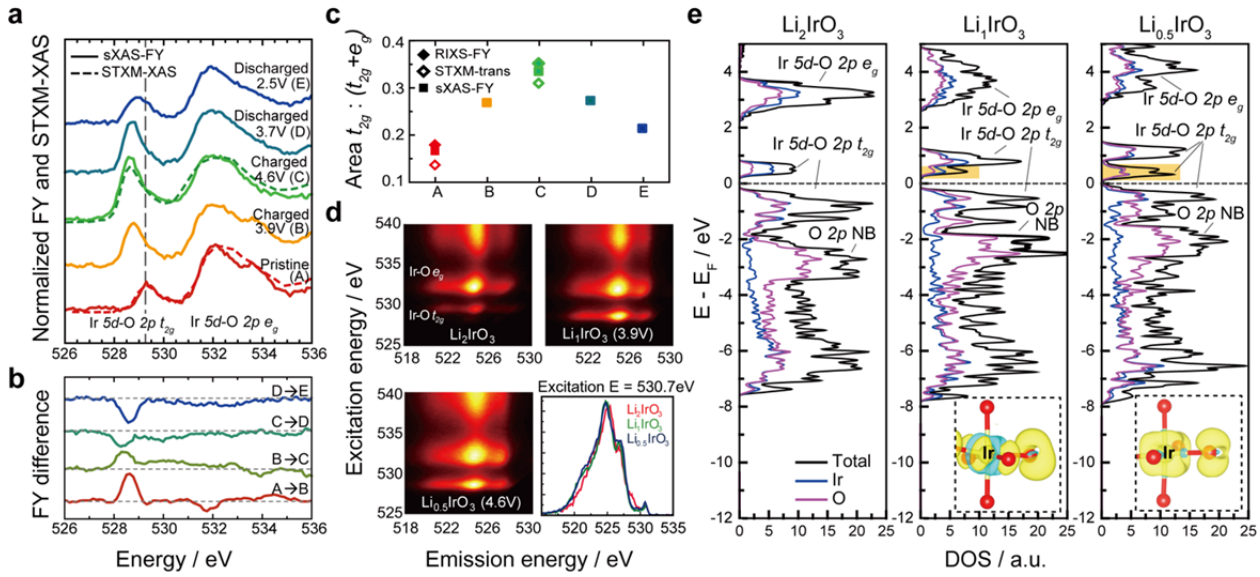

885

886 **Fig. 2**. **Hybridized Ir-O redox in $Li_{2-x}IrO_3$**. (**a**) sXAS fluorescence yield spectra (solid lines)
887 and XAS obtained through scanning transmission X-ray microscopy (STXM-XAS, dashed lines)
888 of the O K edge of $Li_{2-x}IrO_3$ at various voltages throughout the first cycle. From bottom to top,
889 pristine (red, A), charged to 3.9 V (yellow, B), charged to 4.6 V (green, C), discharged to 3.7 V
890 after being charged to 4.6 V (olive, D), discharged to 2.5 V after being charged to 4.6 V (blue,
891 E). (**b**) Difference plot of sXAS obtained from (a) showing the intensity evolution of Ir *5d* -O *2p*
892 t_{2g} and e_g^* peaks. (**c**) Ratio of the Ir *5d*-O *2p* t_{2g} peak area to the total Ir *5d*-O *2p* $t_{2g} + e_g^*$ area
893 measured by RIXS, STXM and sXAS, showing the continuous growth and decay of the t_{2g} area.
894 The O K edge measurements were normalized by the intensity at 545 eV after subtracting the
895 background intensity. (**d**) O K edge RIXS maps of Li_2IrO_3, $LiIrO_3$ and $Li_{0.5}IrO_3$. The right
896 bottom panel shows the RIXS spectra at 530.7 eV excitation energy for each composition where
897 a feature corresponding to anion redox is reported to appear. (**e**) Ir- and O-projected density of
898 states of Li_2IrO_3, $LiIrO_3$ and $Li_{0.5}IrO_3$ calculated from first principles, demonstrating no access to
899 the buried O *2p* non-bonding states. Insets show the isosurface of the charge density for the

900 lowest unoccupied states corresponding to 0.5 electrons/f.u. in $LiIrO_3$ and $Li_{0.5}IrO_3$ (shaded
901 region in (e)) visualizing two different Ir *5d*-O *2p* t_{2g} hybridized states. Yellow and blue show
902 negative and positive changes in charge density, respectively. Li ions are omitted for clarity.
903

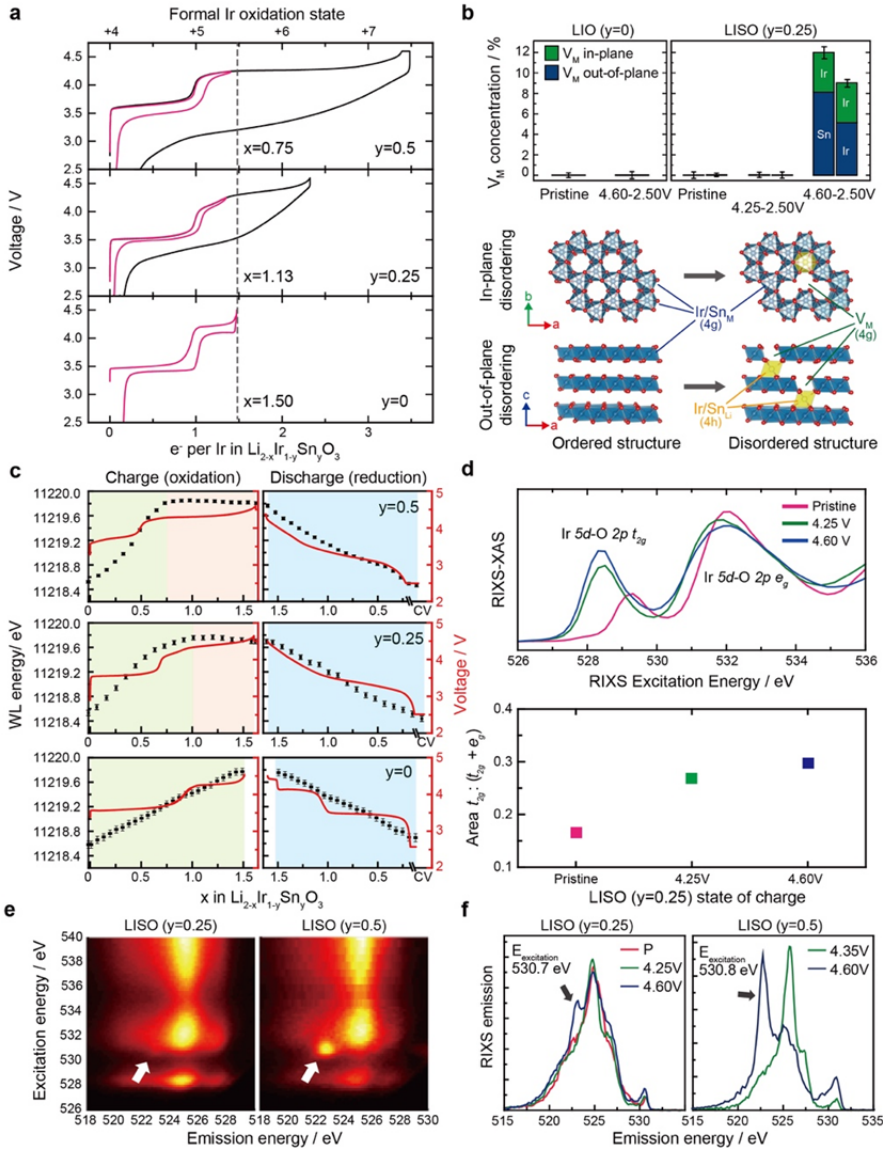

904

905 **Fig. 3**. **Irreversible electrochemistry, structural disordering, and redox behavior of $Li_{2-x}Ir_{1-y}Sn_yO_3$.** (**a**) Charge/discharge profiles of $Li_{2-x}Ir_{1-y}Sn_yO_3$ (y=0, 0.25, 0.5) under a constant current
907 density (C/10 rate) for a full cycle (black) and for an approximately 1.5 electron per Ir per f.u.
908 cycle (pink). (**b**) In-plane and out-of-plane disorder quantified by iterative XRD Rietveld
909 refinement for the LISO25 cycled in the 4.60-2.50 V and 4.25-2.50 V windows and LIO cycled
910 in the 4.60-2.50 V window, quantified by the total V_M concentration. The scheme illustrates the

in-plane (top) and out-of-plane (bottom) structural disordering mechanisms resulting in V_M, with the migrated cation octahedron shaded yellow and the Wyckoff positions indicated in parentheses. (**c**) *Operando* transmission XANES spectra of the Ir L_3 edge for the first cycle showing the continuous Ir oxidation up to 4.25 V, no shift beyond 4.25 V, and the continuous Ir reduction during discharge. (**d**) FY sXAS O K edge spectra (obtained by integrating the RIXS data onto the excitation axis, RIXS-XAS) throughout the first cycle for LISO25 (top) and the corresponding ratio of the Ir *5d*-O *2p* t_{2g} peak area to the total Ir *5d*-O *2p* $t_{2g} + e_g^*$ area (bottom). (**e**) O K edge RIXS maps of LISO25 (left) and LISO50 (right) charged to 4.60 V showing a localized RIXS feature at 530.7 eV excitation energy and 522.8 eV emission energy. (**f**) Single energy RIXS spectra of LISO25 and LISO50 more clearly showing the anion redox signature.

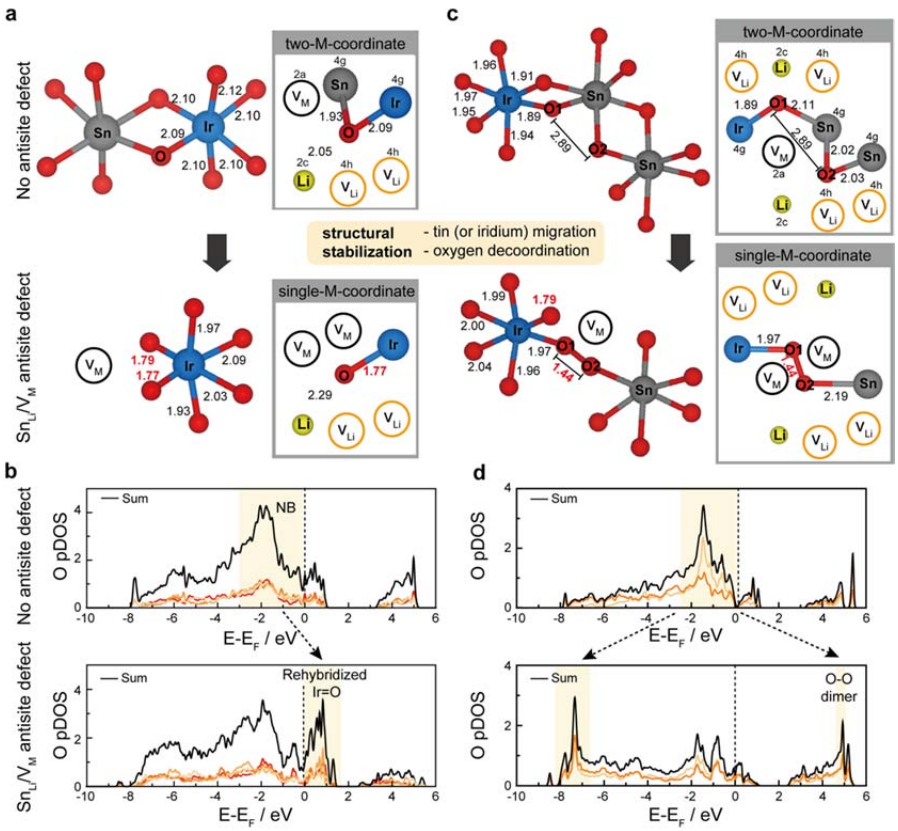

922

923 **Fig. 4. Computational predictions of M-O decoordination and Ir=O/O–O stabilized anion**
924 **redox**. (**a**) Ir–O bond lengths (left) and oxygen coordination environments (right) predicted by
925 DFT in a $Li_{0.5}Ir_{0.75}Sn_{0.25}O_3$ structure before (top) and after (bottom) the formation of a Sn_{Li}/V_M
926 defect when the vacancy neighbors only Ir. Note that the presence of Li neighboring O negligibly
927 affects the O *2p* states due to minimal hybridization between Li and O. (**b**) Projected DOS of the
928 individual oxygen atoms involved in the Ir–O bond contraction before (top) and after (bottom)
929 forming the Sn_{Li}/V_M defect, demonstrating the shift of the O 2*p* states above the Fermi level,
930 indicating oxygen redox. (**c**) Ir–O bond lengths (left) and oxygen coordination environments
931 (right) before (top) and after (bottom) the formation of a Sn_{Li}/V_M defect when the migrating Sn
932 initially neighbors another Sn, resulting in the formation of a 1.44 Å O–O dimer. (**d**) Projected
933 DOS of the individual oxygen atoms involved in the O–O bond formation before (top) and after

(bottom) forming the Sn_{Li}/V_M defect and O–O dimer, also showing a shift of the O 2*p* states above the Fermi level.

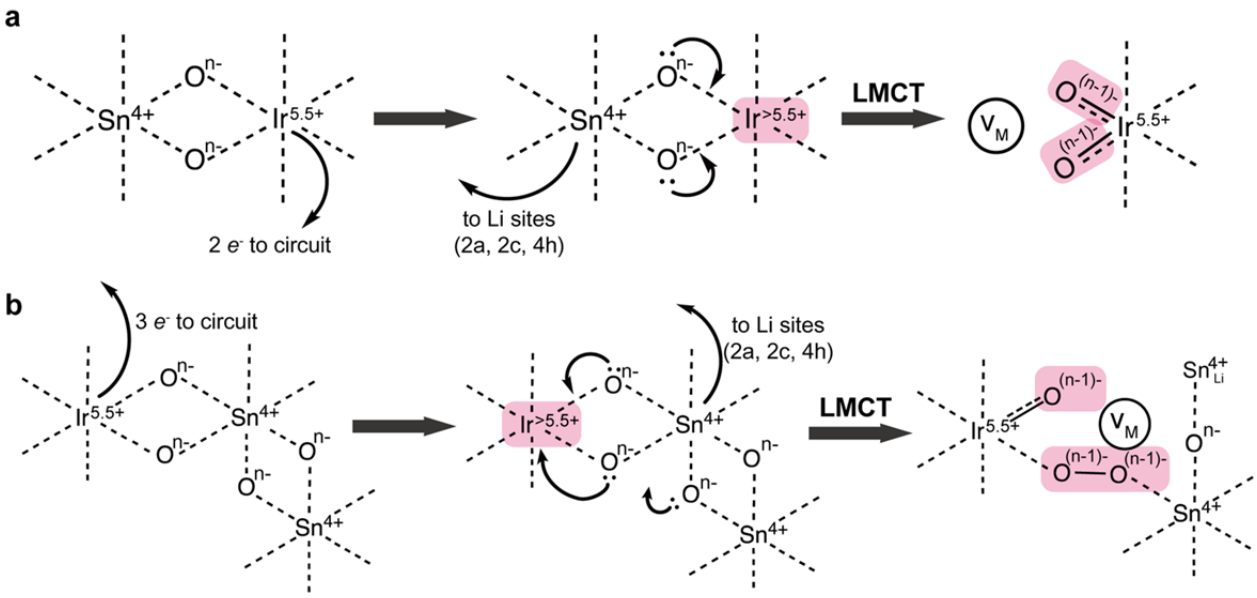

937

938 **Fig. 5**. **Proposed electronic mechanism of cation migration and LMCT mediated anion**
939 **redox in LISO.** (**a**) The mechanism of Ir=O formation, wherein Ir is initially oxidized beyond
940 $Ir^{5.5+}$, promoting LMCT *via* Sn migration, oxygen decoordination, and donation of oxygen lone
941 pair (unhybridized O 2*p*) electrons to forming a short Ir–O π bond. Each black arrow corresponds
942 to the redistribution of an electron pair. **(b)** The mechanism of O–O formation when a dangling
943 O is coordinated to a Sn atom, wherein LMCT is achieved instead through donation of the O–O
944 σ* electrons to Ir. Both cases assume that the number of electrons provided through LMCT
945 mediated oxygen redox is equal to the number of decoordinated oxygens. Note that the
946 calculations in Fig. 4 reflect only the LMCT step in both cases.